RSC Advances

PAPER

View Article Online
View Journal | View Issue

Cite this: *RSC Adv.*, 2026, **16**, 21570

Multifunctional Ag-doped CuS surface nanostructures for simultaneous dye degradation and bacterial inactivation *via* visible-light activation

Nissren Tamam,[a] Kashif Ali,[b] Salma Saddeek,[c] Tasneem I. Hussein,[d] Mazen R. Alrahili,[e] Imran Shakir,[f] Muawya Elhadi[g] and Muhammad Aadil *[h]

This work reports a new dual-strategy approach for the preparation of nanostructured Ag-doped CuS ($Cu_{1-x}Ag_xS$, $x = 0.03$) photocatalysts designed by the synergy of morphology control and band gap engineering for enhanced environmental cleanup. The hexagonal covellite phase, the successful lattice substitution of Ag ions, and the change from strongly agglomerated 65 nm particles to well-dispersed 55 nm nanoparticles were confirmed by systematic characterization using XRD, FTIR, SEM, and EDX analyses. In addition, *I–V* analysis demonstrated a remarkable increase in conductivity. Together with UV-vis DRS, PL, electrochemical impedance spectroscopy (EIS), and transient photocurrent response analyses, the results demonstrated that Ag doping decreased the bandwidth from 1.69 eV to 1.57 eV, strongly inhibited charge recombination, and improved interfacial charge transfer. Thus, 3% Ag-doped CuS with the best performance shows excellent photocatalytic activity, with almost 98.2% MB degraded in 80 min ($k = 0.029$ min^{-1}), which is 3.6 times higher than the activity of pristine CuS. In addition, an anti-bacterial assay revealed a 2.12-fold increase in the zone of inhibition against *Escherichia coli* (23.3 mm). Mechanistic information based on radical scavenging experiments and electron paramagnetic resonance (EPR) spectra indicated that $^{\bullet}OH$ and $^{\bullet}O_2^-$ were the major reactive species for dye mineralization and bacterial inactivation. Cyclic degradation experiments and after-cycling XRD analysis demonstrated that the material could be reused several times without any structural degradation.

Received 23rd March 2026
Accepted 7th April 2026

DOI: 10.1039/d6ra02367c

rsc.li/rsc-advances

1 Introduction

The development of industries and the medical sector guarantees human development and human health security. Unfortunately, most industries, including textile, leather, paint, food, cosmetic, hospital and pharmaceutical units, directly discharge their effluents into natural water bodies without treatment.[1] These industrial discharges, which mainly consist of several organic and inorganic pollutants, *i.e.*, synthetic dyes, mineral acids, pesticides, antibiotics, hexavalent chromium, other heavy metals, and pathogenic microorganisms, severely endanger aquatic life and human beings when they enter the food chain.[2,3]

Pollution of water sources also affects the agricultural sector, leading to a loss of crop quality and quantity due to irrigation with contaminated water. In addition, the consumption of contaminated water without treatment promotes the dissemination of a number of fatal water-borne diseases such as cholera and typhoid.[4] The environmental and human health risks are further exacerbated by non-biodegradable, carcinogenic organic dyes and antibiotic residues, which can promote the growth of multiple-drug-resistant bacteria.[5] As a result, before the disposal of polluted water into natural waterways, it is important to treat the water, particularly for the inactivation of pathogenic microbes (bacteria) and the degradation of synthetic dyes.[6] Thus, there is an urgent need for innovative approaches to simultaneously combat bacterial proliferation and remove recalcitrant dyes. Many different processes have been implemented to remove integrated pollutants (dyes and pathogenic microbes) from ecosystems. These include physical processes (*e.g.*, sedimentation, adsorption, flocculation, and filtration), chemical methods (*e.g.*, ozone and ion exchange),

[a]*Department of Physics, College of Science, Princess Nourah bint Abdulrahman University, P.O. Box 84428, Riyadh, 11671, Saudi Arabia*
[b]*Division of Science and Technology, Department of Zoology, University of Education, Lahore, Pakistan*
[c]*Department of Chemistry, Faculty of Sciences, University of Hafr Al Batin, Hafr Al Batin 39524, Saudi Arabia*
[d]*Department of Chemistry, College of Science, Qassim University, Buraydah, 51452, Saudi Arabia*
[e]*Department of Physics, College of Science, Taibah University, Madinah, Saudi Arabia*
[f]*Department of Physics, Faculty of Science, Islamic University of Madinah, Madinah, 42351, Saudi Arabia*
[g]*Department of Physics, Faculty of Science and Humanities, Shaqra University, P. O. Box 1040, Ad-Dawadimi, 11911, Saudi Arabia*
[h]*Department of Chemistry, Rahim Yar Khan Campus, The Islamia University of Bahawalpur, Rahim Yar Khan 64200, Pakistan. E-mail: Muhammad.aadil@iub.edu.pk*

and biological processes (*e.g.*, bioremediation and activated sludge).[7–9] Unfortunately, each of these conventional techniques has several limitations, including high operational costs, the generation of hazardous secondary residues, low efficiency, and the need for extreme operating conditions (*e.g.*, very high pressures or temperatures).[10]

Photocatalysis is increasingly considered a green alternative to conventional methods for wastewater treatment, as structurally modified semiconductor photocatalysts can efficiently produce electron–hole pairs upon irradiation with photons of energy greater than their band gap.[11,12] These charge carriers then interact with oxygen and water, forming reactive oxygen species (ROS).[13] The ROS chemically interact with toxic dyes later on, annihilate them into non-polluting final products, and enhance bacterial inactivation by damaging intracellular components.[14] Transition metal sulfides can serve as efficient photocatalysts on account of their adjustable band gaps and natural availability on Earth,[15] but their serious application is restricted by fast charge carrier recombination and inferior charge transport kinetics.[16,17]

There are many ways of enhancing catalytic performance, including doping, composites, and heterojunctions.[18–20] Copper sulfide is an n-type semiconductor photocatalyst. In its pristine form, its photocatalytic activity is limited because of its limited light-harvesting and fast charge recombination.[21] The doping strategy has attracted attention for improving the bandgap for better light harvesting and charge separation/conductivity. Report after report shows the value of doping. Many reported works disclose the importance of doping in photocatalysis. Vinotha *et al.* successfully achieved 98% degradation of rhodamine B (RhB) with indium-doped CuS,[22] while Cao *et al.* synthesized nanotube-like Zn-doped CuS with improved light absorption and thermal stability and successfully achieved 96% degradation of MB.[23] Ahmad *et al.* synthesized hexagonal In-doped CuS nanoparticles that showed superior antimicrobial activity against *Mycobacterium smegmatis*.[24]

Herein, we present a hydrothermal approach for the preparation of novel Ag-doped CuS ($Cu_{1-x}Ag_xS$) nanostructures that can be utilized as a unique multifunctional platform. After thorough physicochemical analysis, the bifunctional remediation potential of the material was assessed by means of the dye methylene blue (MB), an obstinate textile dye, and *Escherichia coli*, a common pathogenic bacterium. This new single-matrix concept could lead to dual-therapy treatment for the simultaneous removal of organic contaminants and microbial agents from challenging wastewater solutions. This new single-matrix concept could lead to dual-therapy treatment for the simultaneous removal of organic contaminants and microbial agents from challenging wastewater solutions.

2 Experimental section

2.1 Chemicals

Copper(II) nitrate trihydrate [$Cu(NO_3)_2 \cdot 3H_2O$], thiourea (CH_4N_2S), and silver nitrate ($AgNO_3$) with high purity (>99%) were sourced from Sigma-Aldrich. The synthesis was conducted using deionized water.

2.2 Synthesis of Ag-doped CuS

In order to prepare 3 mol% silver-doped CuS ($Cu_{1-x}Ag_xS$, where $x = 0.03$) NPs, a solution containing 2.345 g (10 mmol) of copper(II) nitrate trihydrate and 0.051 g (0.3 mmol) of silver nitrate was prepared and stirred. Then, 40 mL of deionized water was added to thiourea (0.761 g, 0.01 mol), and the mixture was stirred for 25 minutes. The thiourea solution was slowly added to the metal precursor solution while stirring until a homogeneous mixture formed, after which all the material was transferred to the autoclave and heated for 18 h at 180 °C. The precipitate was centrifuged after cooling to room temperature, then carefully washed with deionized water and ethanol until the liquid reached a neutral pH. $Cu_{1-x}Ag_xS$ nanopowder was dried overnight in an oven at 80 degrees Celsius. Undoped CuS nanoparticles were synthesized using the same technique, with the difference that the silver nitrate was removed from the precursor solution. The 1 mol%, 3 mol%, and 5 mol% Ag-doped CuS samples were synthesized and characterized to determine the best photocatalyst. Of all of them, the 3 mol% Ag-doped sample showed the strongest visible-light absorption and charge separation efficiency; thus, further studies concentrate on this optimized composition.

2.3 Photocatalytic experiment

The photocatalytic efficacies of pure CuS and doped $Cu_{1-x}Ag_xS$ were examined using MB as a model contaminant. Each catalyst was individually dispersed at a dosage of 10 mg in 50 mL of a methylene blue solution (5–25 ppm). The suspensions were stirred in the dark to reach a balance between desorption and adsorption after 30 minutes. When equilibrium was achieved, a sample of the suspension was removed to obtain the initial absorbance using a UV-vis spectrophotometer. A tungsten filament lamp was used to expose the catalyst-dye solution to visible light. The time exposure for $Cu_{1-x}Ag_xS$ was 80 minutes and that for pure CuS was 90 minutes. At 10 min intervals, aliquots (5 mL) were taken off and centrifuged, and the supernatants were analyzed for MB at its maximum absorption wavelength by UV-visible spectrophotometry. The equation given below was used to calculate the degradation efficiency:[25]

$$\%\ \text{Photodegradation} = [(C_0 - C_t)/C_0] \times 100.$$

In this equation, C_t represents the absorbance at time $= t$ min, while C_0 represents the starting absorbance at $t = 0$ min.

3 Results and discussion

3.1 XRD and FTIR

The crystalline structure of the synthesized nanomaterials was confirmed by X-ray diffraction studies. The XRD patterns of the freshly synthesized CuS and $Cu_{1-x}Ag_xS$ samples are shown in Fig. 1a. Seven sharp and well-defined diffraction peaks were observed in the XRD pattern of the unmodified CuS. These peaks, recorded at 2θ values of 27.9°, 29.5°, 32.0°, 33.25°, 48.4°, 53.2°, and 59.9° respectively correspond to the (101), (102), (103), (006), (110), (108), and (116) planes. These planes are in excellent

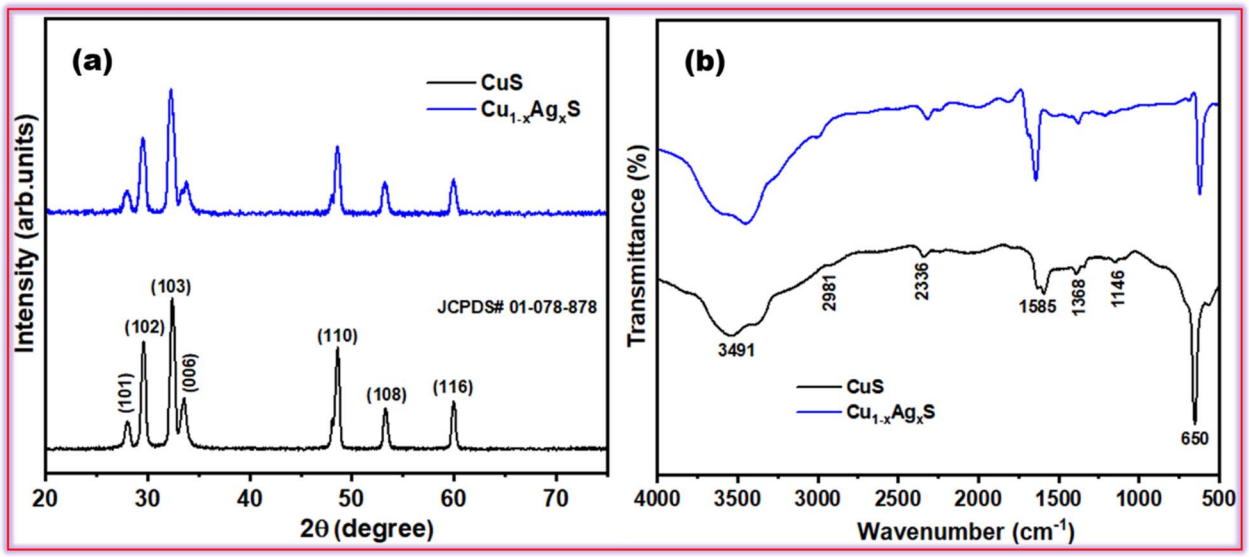

Fig. 1 (a) XRD patterns and (b) FTIR spectra of CuS and $Cu_{1-x}Ag_xS$.

agreement with JCPDS no. 01-078-0878,[26] confirming the synthesized hexagonal covellite-phased CuS. The observed X-ray diffraction pattern of the doped sample shows all the characteristic diffraction peaks of the hexagonal covellite structure of CuS. This confirms that the incorporation of Ag ions into the CuS lattice substitutes Cu^+ ions within the lattice without forming any secondary phases.[27] In contrast, the XRD peaks of the doped sample are less intense, relatively broadened, and shifted towards lower diffraction angles compared to the CuS diffraction peaks. The decline in the peaks' intensity is ascribed to a decrease in crystallinity, possibly due to structural defect creation,[28,29] the peak broadening clearly suggests a decrease in the crystallite size, possibly due to limited grain boundary growth and controlled nucleation, while the peak shifting suggests lattice expansion, possibly due to the substitution of smaller Cu^+ ions (0.77 Å) by bigger Ag^+ ions (1.26 Å), as predicted by Bragg's law.

The findings from the FTIR analysis (Fig. 1b) support key insights regarding the chemical bonding and also provide key information about the surface chemistry. The FTIR spectrum for pristine CuS (*i.e.*, CuS without any dopants) shows an intense Cu–S vibrational band at 650 cm^{-1}, which confirms that copper sulfide was successfully formed during synthesis.[30] In addition to the Cu–S vibrational band, the FTIR spectrum of pristine CuS shows secondary transmission bands of relatively low intensity, including C–H vibrations (1146 cm^{-1}, 2981 cm^{-1}),[31–33] nitrate remnants (1368 cm^{-1}),[34] O–H vibrations that correspond to adsorbed water (1585 cm^{-1}, 3491 cm^{-1}),[35,36] and atmospheric CO_2 (2336 cm^{-1}).[37] The spectrum of the $Cu_{1-x}Ag_xS$ retains all of its characteristic peaks (confirming its structural integrity); however, the main Cu–S band (peaking at approximately 627 cm^{-1}) shifts to lower wavenumbers and is less intense as a result of bond elongation and weakening due to the larger Ag^+ ions effectively replacing Cu^+ cations (which are smaller).[38] In addition, peaks corresponding to adsorbed water and CO_2 become more pronounced, indicating that the Ag dopant enhances surface porosity and active sites.

3.2 SEM and EDX

We conducted a SEM analysis to study the surface topography, surface defects, particle size, and particle distribution of the synthesized CuS and $Cu_{1-x}Ag_xS$ samples. The SEM micrograph of the CuS sample (Mag. 40 500×), shown in Fig. 2a, indicates that the sample has quasi-spherical agglomerated nanoparticles of uneven distribution. The inset histogram in Fig. 2a indicates that the nanoparticles of CuS are between 62 and 69 nm, with an average size of 65 nm. Fig. 2b shows the $Cu_{1-x}Ag_xS$ sample's SEM micrograph taken at a magnification of 42 000×. The Ag-doped CuS exhibits spherical nanoparticles in a well-dispersed state, reducing aggregation. The inset histogram in Fig. 2b shows a smaller particle size range of 53–57 nm, with a reduced average particle size of 55 nm. The doped sample demonstrated greater morphological consistency, smaller particle size, and better dispersion, resulting in a larger surface area. This enables more effective pollutant adsorption and increased photocatalytic effectiveness.[39]

The elemental compositions of pure and Ag-doped CuS were determined using EDX. The EDX spectra for both synthesized samples are shown in Fig. 2c. The EDX spectrum of virgin CuS displayed four unique peaks: three associated with copper (Cu) at 0.93 keV (Lα), 8.04 keV (Kα), and 8.90 keV (Kβ) and a significant peak at 2.31 keV (Kα) attributable to sulfur (S).[40] In contrast, the EDX spectrum of $Cu_{1-x}Ag_xS$ (Fig. 2d) not only retains the original peaks of copper and sulfur but also has additional peaks at ~3.0 keV (Lα), confirming the presence of silver (Ag) as a dopant.[41] Statistical analysis of the $Cu_{1-x}Ag_xS$ sample's EDX spectrum showed 49.10 at% (63.95 wt%) for copper and 49.23 at% (32.35 wt%) for sulfur, while silver accounted for only 1.67 at% (3.70 wt%).

3.3 Optical and electronic characterization

The synthesized nanomaterials' optical characteristics were analyzed by UV-vis DRS to establish the effect of Ag substitution

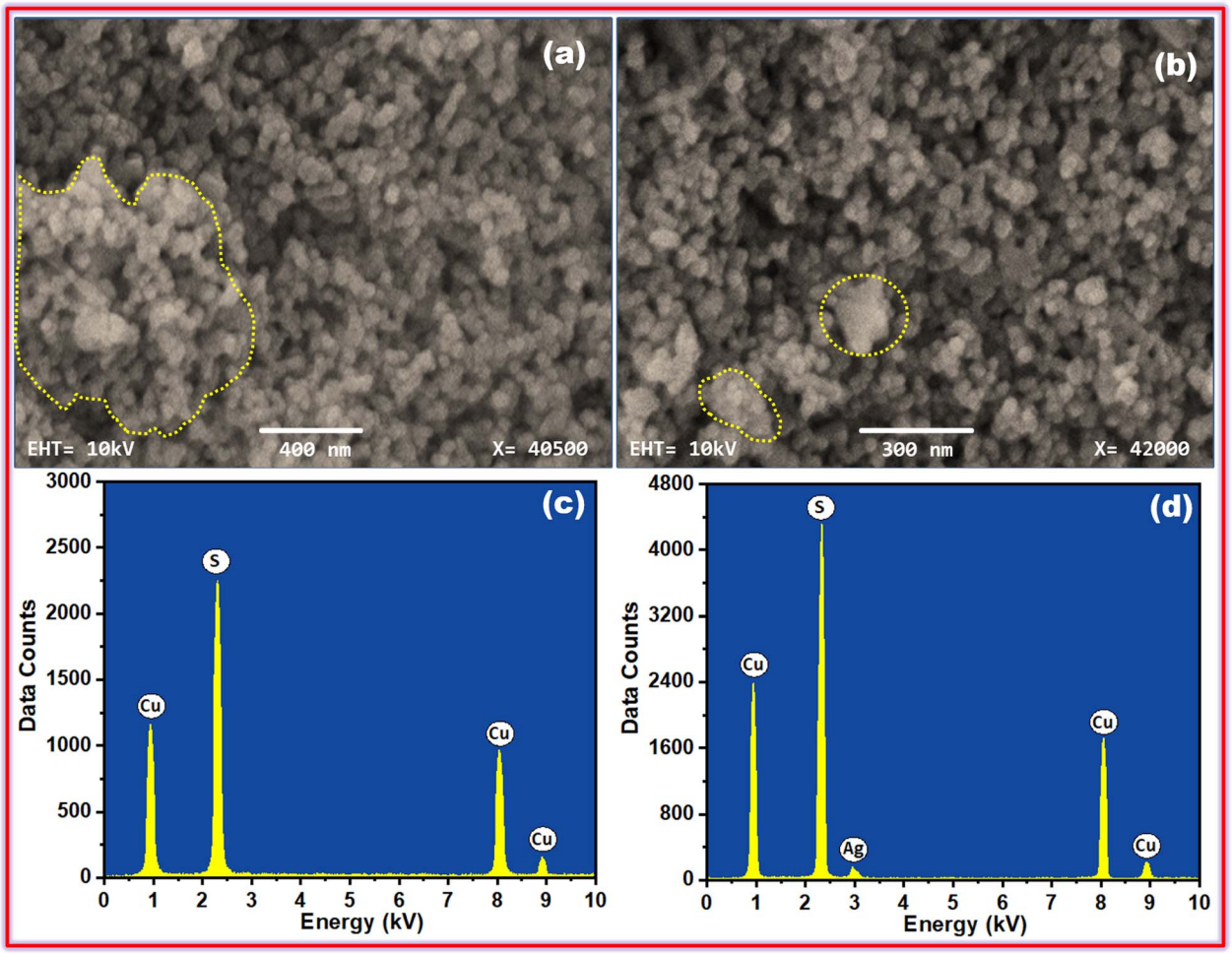

Fig. 2 (a) SEM image of CuS and (b) SEM image of $Cu_{1-x}Ag_xS$. (c) EDX results of CuS and (d) EDX results of $Cu_{1-x}Ag_xS$.

on the electronic structure and light-harvesting ability. As shown in Fig. 3a, the $Cu_{1-x}Ag_xS$ displays a distinct bathochromic shift of its absorption edge with respect to pristine CuS.[42] This qualitative change indicates the high ability of the material to harvest photons from the visible range of the electromagnetic spectrum, which is important for visible-light-driven applications, *i.e.*, photocatalysis. Tauc plots were extracted from the Kubelka–Munk function to quantify this electronic modulation.[43] The inception of Ag ion doping in the CuS is analyzed and clearly reduces the optical band gap energy considerably, with the band gap energy for undoped CuS found to be 1.69 eV and that for Ag-doped CuS being 1.57 eV (Fig. 3b).

The finding of this 0.12 eV narrowing may be an important observation and can be attributed to the Ag-induced intermediate energy states in the forbidden band gap. These states lower the energy needed for electron transitions, thus creating charged particles through the reaction with photons of lesser energy. The improved photocatalytic performance is mainly due to this strategic band gap engineering. The narrow band gap directly relates to the higher generation rate of photogenerated electron–hole pairs (e^-–h^+) under visible-light irradiation. Also, the doped Ag^+ ions can function as helpful electron-trapping sites, which spatially separate charge carriers and reduce their recombination. The improved photocatalytic degradation and antibacterial inactivation by the Ag-doped CuS nanocatalyst can be attributed to the enhanced light absorption and better charge separation dynamics, resulting in its superior efficiency. PL spectroscopy was employed to investigate charge-carrier dynamics. The intensity of the emission from $Cu_{1-x}Ag_xS$ was much lower than that from CuS, as can be seen in Fig. 3c. This means that the recombination rate of e^-–h^+ photogenerated in $Cu_{1-x}Ag_xS$ is much lower compared to that in CuS.[44] The strong emission band of the CuS sample is centered above 600 nm, which may be ascribed to the band-edge emission, while for the $Cu_{1-x}Ag_xS$, this band shows a red shift and is observed above 650 nm, indicating that Ag doping has successfully tuned the band structure. Notably, the PL spectrum of the doped sample shows a pronounced hump at higher wavelengths, which may be attributed to defect-state-derived emissions.[45] Ag doping not only reduced the band gap to maximize quantum efficiency but also acted as an electron-trap center, prolonging charge-carrier lifetimes and making them available for surface redox reactions.[46]

I–V analysis was used to assess the effect of silver doping on charge transport. As shown in Fig. 3d, the charge transport in $Cu_{1-x}Ag_xS$ is greatly improved, as indicated by the increased slope of the *I–V* curve. Based on the modified Ohm's law, the increased

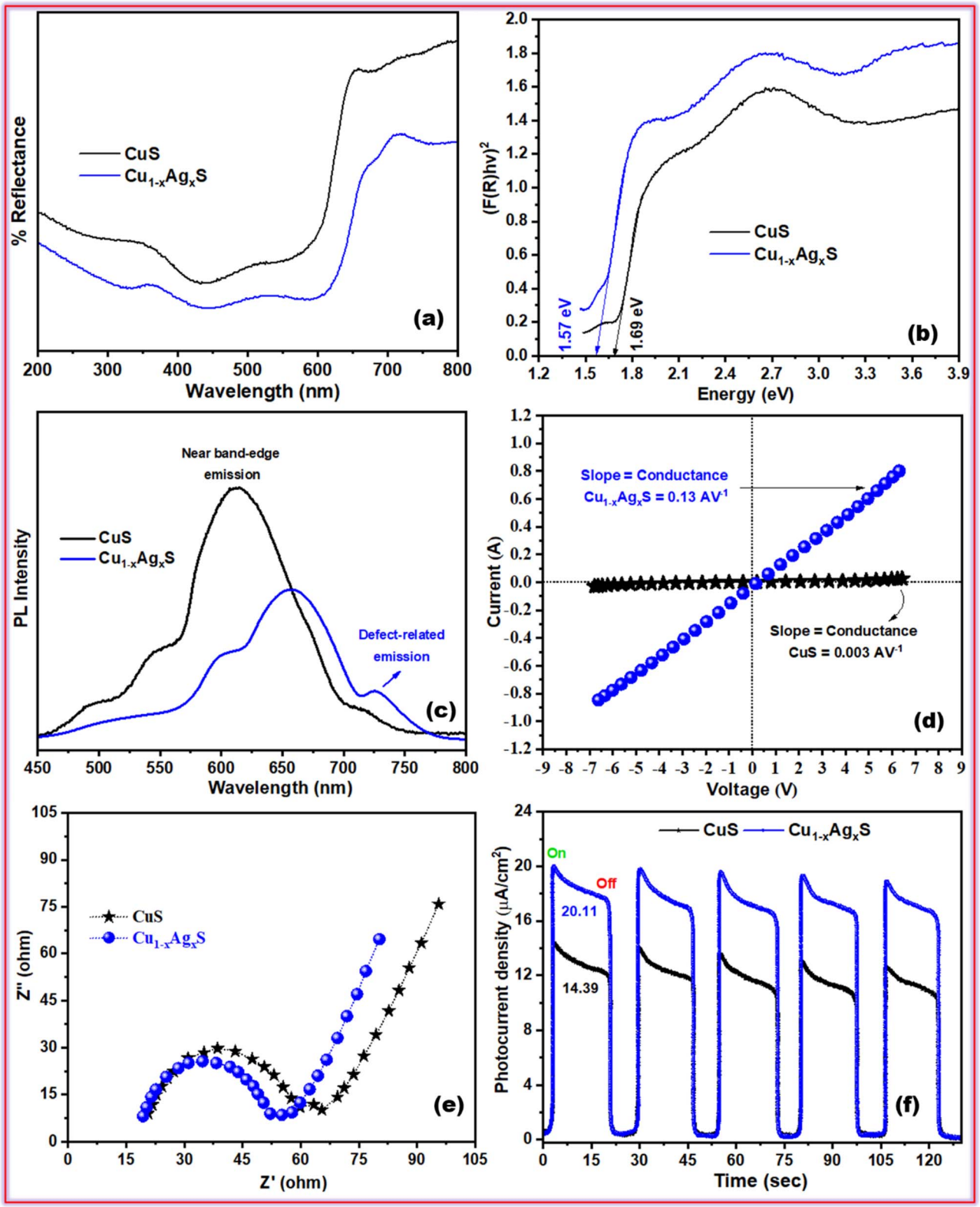

Fig. 3 (a) UV-vis reflectance spectra, (b) Tauc plots, (c) PL spectra, (d) *I–V* profiles, (e) EIS plots, and (f) transient photocurrent responses of CuS and $Cu_{1-x}Ag_xS$.

slope indicates greatly improved electrical conductance.[47,48] The greater improvement in conductance for $Cu_{1-x}Ag_xS$ can be ascribed to the changes in the local electronic environment caused by the partial replacement of Cu^+ ions with Ag^+ ions. The partial replacement of Cu^+ ions with Ag^+ ions makes it easier to transport charge carriers to the catalytic surface.

In addition, electrochemical impedance spectroscopy (EIS) and transient photocurrent response were performed to further understand the charge transfer kinetics. As shown in Fig. 3e, the arc radius of the Nyquist plot for the $Cu_{1-x}Ag_xS$ sample is much smaller than that of the pristine CuS. The decrease in the diameter of the semicircle represents the decrease in the charge transfer resistance at the interface of the electrode/electrolyte and faster interfacial charge transport.[49] In line with this, the transient photocurrent response in Fig. 3f demonstrates that the Ag-doped sample has significantly larger photocurrent density under visible light irradiation. The increased photocurrent further validates the efficient inhibition of e–h recombination and the rapid charge migration, also confirming the highest photocatalytic activity of the doped nanocatalyst.[50,51]

3.4 Antimicrobial activity

As shown in Fig. 4a and b, the antibacterial activities of the CuS and $Cu_{1-x}Ag_xS$ nanocatalysts on the growth of the bacterium *Escherichia coli* were determined through the agar-well diffusion method. After incubation at 37 °C for 24 hours, both samples showed concentration-dependent antibacterial behavior, and $Cu_{1-x}Ag_xS$ was significantly more bactericidal at all concentrations tested (4–16 μg). For the optimal concentration of 16 μg, $Cu_{1-x}Ag_xS$ registered a markedly larger inhibition zone of 23.3 mm, which is 2.12 times the inhibition zone of 11 mm for the undoped CuS (Fig. 4c). The antibacterial mechanism for both materials is based on the photocatalytic generation of reactive oxygen species (ROS) upon visible-light irradiation (Fig. 4d). However, the antibacterial effect of CuS is inferior to that of $Cu_{1-x}Ag_xS$ owing to the lack of defect states or Ag+ states, leading to a high rate of charge recombination that reduces the total ROS population and limits its activity. In comparison, the enhanced and synergistic antibacterial performance of $Cu_{1-x}Ag_xS$ can be attributed to the introduction of Ag^+ ions into the CuS lattice that intensifies photocatalysis from several aspects:[52] (1) narrowing the bandgap down to 1.57 eV makes better use of visible light for higher efficiency, (2) Ag^+ ions serve as an electron trapping site

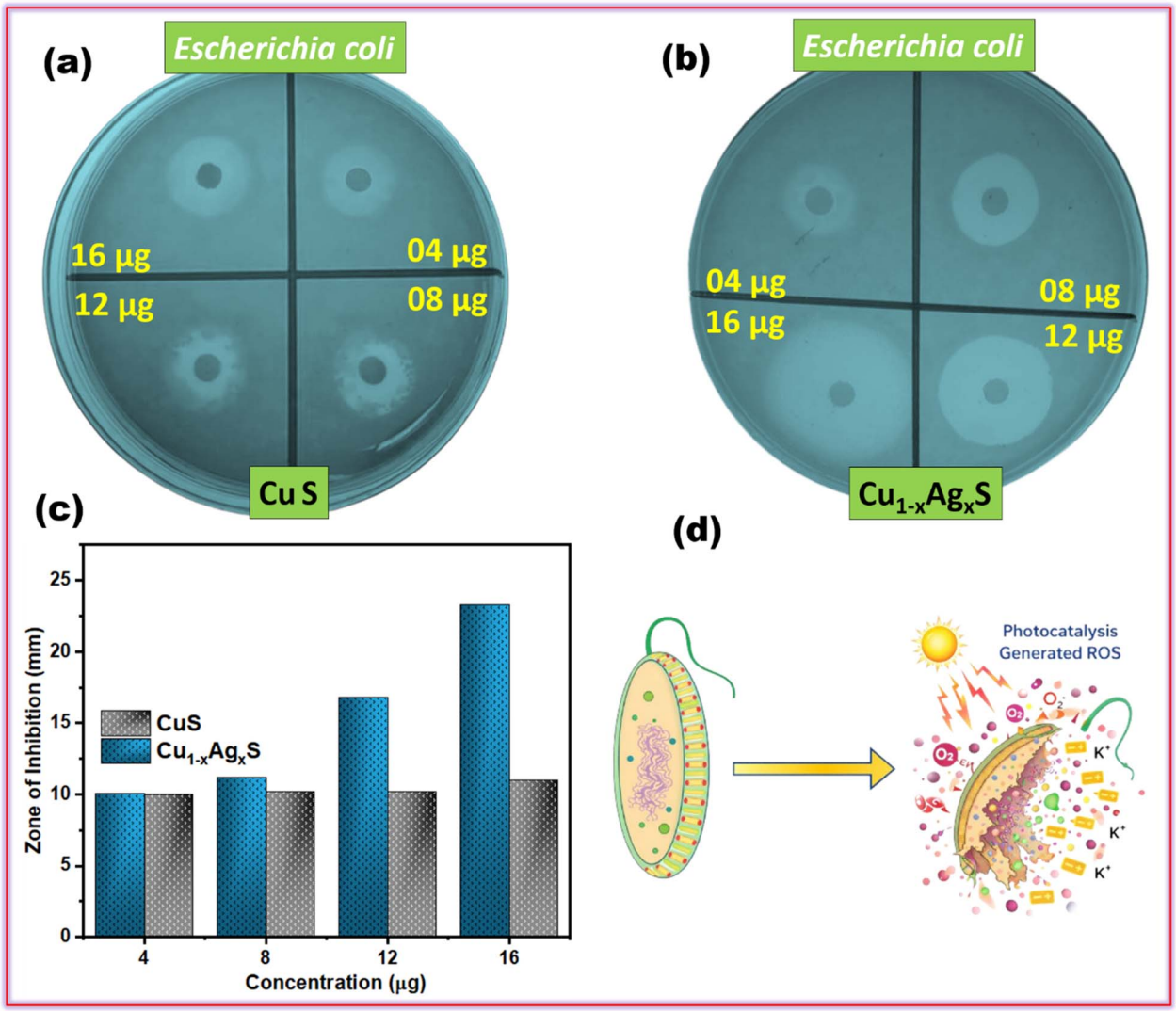

Fig. 4 Antibacterial activities of (a) CuS and (b) Ag-doped CuS. (c) Zone of inhibition comparison between CuS and Ag-doped CuS. (d) Photocatalytic destruction of *E. coli*.

that reduces interfacial charge recombination, thus prolonging exciton lifetimes, and (3) extra antimicrobial behavior is associated with controlled release of Ag^+ ion.

3.5 Dye degradation activity

The photocatalytic activities of the pure CuS and $Cu_{1-x}Ag_xS$ nanocatalysts were systematically assessed using methylene blue (MB) as a model organic pollutant. The degradation process can be defined as two sequential steps: an initial stage of physical adsorption followed by photoinduced catalytic degradation. To achieve adsorption–desorption equilibrium, the catalyst-dye suspensions were swirled in the dark for 30 minutes before irradiation. UV-vis spectra at the characteristic absorbance of MB (665 nm) clearly revealed that the Ag-doped sample had a better adsorption capacity (11.5%) than the undoped CuS (6.4%) (Fig. 5a and b). This enhancement is attributed to the higher surface-to-volume ratio and the suitable surface morphology of the $Cu_{1-x}Ag_xS$ nanocatalyst.[53]

Later, dye-degradation tests under light irradiation with a photocatalyst showed that the $Cu_{1-x}Ag_xS$ photocatalyst exhibited superior photocatalytic activity compared to bare CuS. Time-resolved UV-vis spectra showed that the degradation rate of $Cu_{1-x}Ag_xS$ was much faster, with 98.2% of total methylene blue (MB) degraded in 80 minutes (86.7% *via* photodegradation). CuS, in contrast, took 90 minutes to reach 53.1% (46.7% by photodegradation) removal (Fig. 5c). The observed significant improvement in the degradation efficiency of the $Cu_{1-x}Ag_xS$, almost 45.1% higher than that of bare CuS, can be directly attributed to the synergistic effect of incorporating Ag^+: a reduced band gap (1.57 eV *versus* 1.69 eV) enables easier access to visible light, and an increase in charge-separation efficiency reduces electron–hole recombination.

Kinetic analysis showed that the degradation of MB over both catalysts follows the pseudo-first-order kinetic model, and the correlation coefficients for the degradation process are high (Adj. $R^2 > 0.97$ in $Cu_{1-x}Ag_xS$ and 0.99 in CuS) as follows:[54]

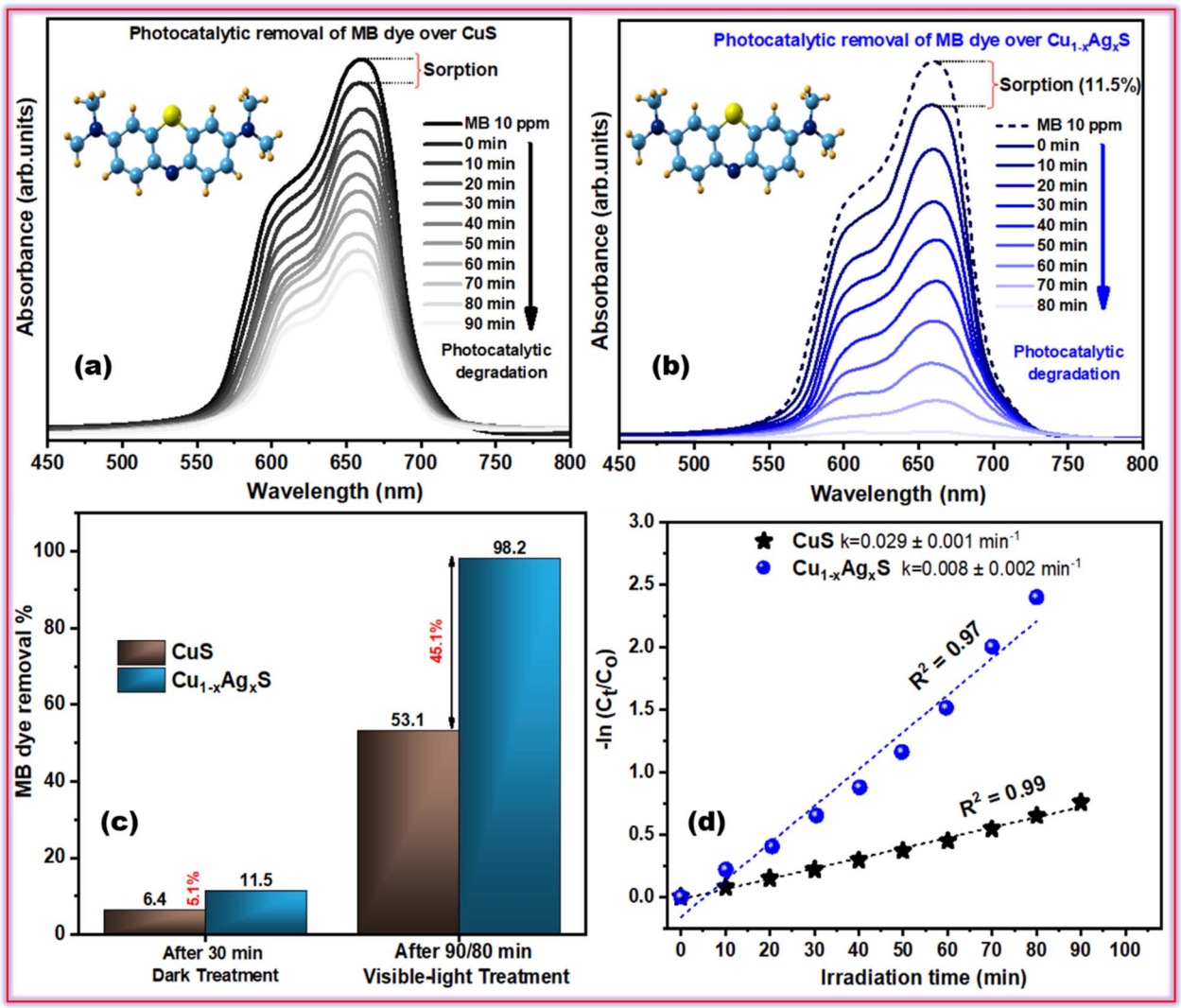

Fig. 5 Photocatalytic degradation of MB dye over (a) CuS and (b) $Cu_{1-x}Ag_xS$. (c) Comparative bar chart of the total removal efficiencies. (d) Pseudo-first-order kinetic plots illustrating the significantly enhanced degradation rate of $Cu_{1-x}Ag_xS$.

$$-\ln (C_t/C_0) = kt.$$

The rate constant of $Cu_{1-x}Ag_xS$ (0.029 min^{-1}) is also 3.6 times greater than that of pure CuS (0.008 min^{-1}) (Fig. 5d), which definitely proves the catalytic superiority of the Ag-modified system.[38] These results support $Cu_{1-x}Ag_xS$ as a highly efficient visible-light-active photocatalyst in which the dual enhancement strategy, involving morphological optimization and band gap engineering, yields a synergistic effect that is much more efficient than the undoped version. The outstanding photocatalytic activity together with its proven antibacterial properties make $Cu_{1-x}Ag_xS$ a promising, versatile nanomaterial for a wide range of wastewater remediation processes.

3.6 Photocatalytic process optimization

The key operating conditions (MB dye concentration, $Cu_{1-x}Ag_xS$ dosage, pH, and temperature) for the $Cu_{1-x}Ag_xS$-driven MB dye degradation reaction were optimized by studying their effects on the rate constant, as shown in Fig. 6a–d. The initial MB concentration had a significant impact on degradation productivity, and the optimal concentration (10 ppm) removed 98.2% (Fig. 6a). This concentration effect can be explained by the equilibrium between active sites and the photon penetration depth: below 10 ppm, the concentration is too low to allow full utilization of the catalyst; above that level, the light is screened, and the active sites become saturated.[55,56] The loading of catalysts showed a volcano-shaped dependence of the degradation efficiency, with a peak at 10 mg (98.2% removal) (Fig. 6b). However, catalyst overload (>10 mg) causes agglomeration (particle light scattering) and reduces the efficiency of photon utilization, thereby reducing the degradation rate.[57]

The pH of the solution is one of the important characteristics that will affect the physical interaction between the catalytic surface and the MB molecules. The photocatalytic activity is at its maximum at a pH of 9 with $k = 0.029$ min^{-1} (Fig. 6c). In alkaline conditions, the $Cu_{1-x}Ag_xS$ surface will have a hydroxyl negative charge, leading to an efficient electrostatic interaction with cationic MB dye, enabling efficient electron transfer. Meanwhile, the present resources of OH^- serve as the precursor

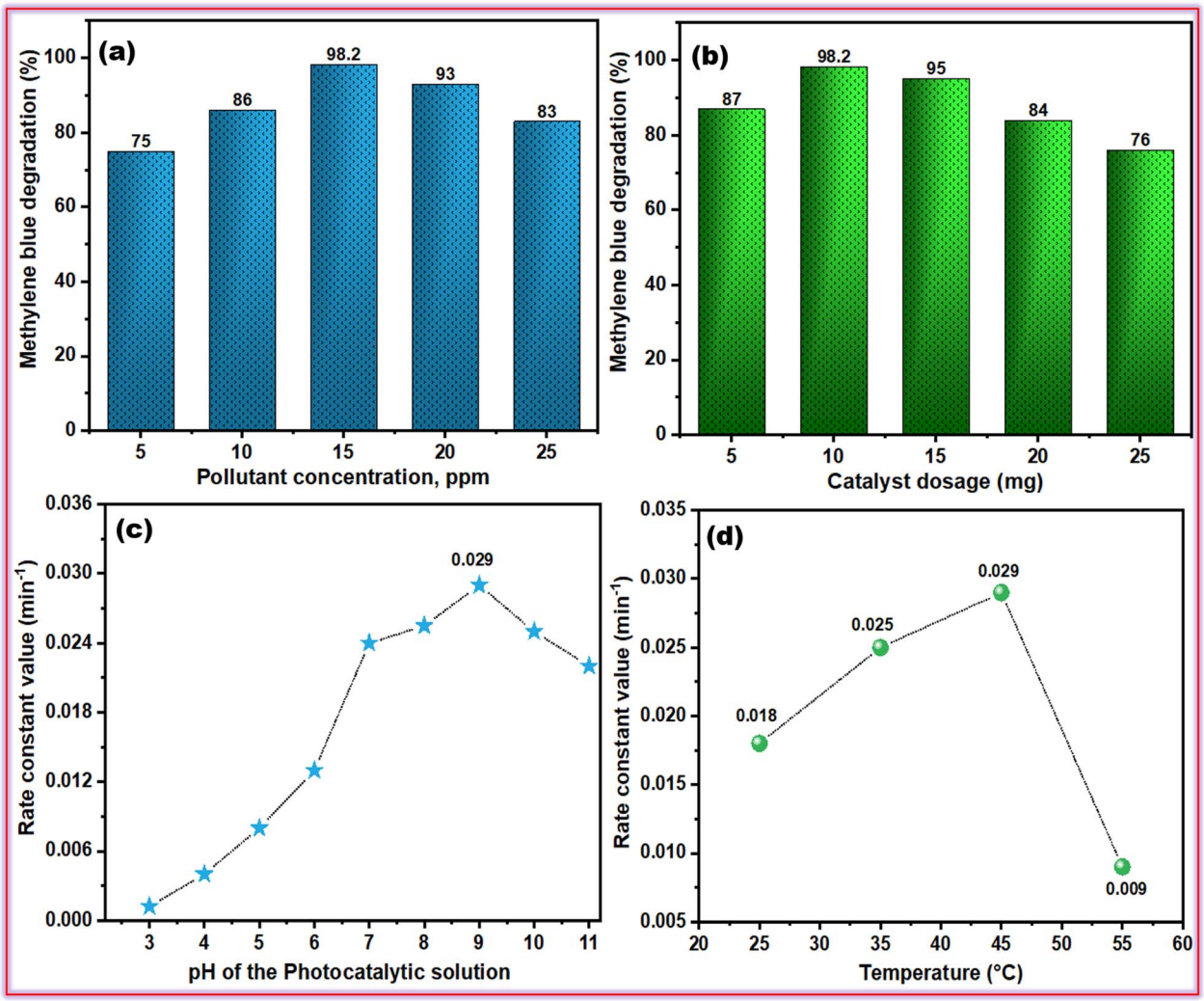

Fig. 6 Effects of (a) MB dye concentration, (b) catalyst dosage, (c) pH value, and (d) temperature on the photocatalytic rate constant for MB dye degradation using $Cu_{1-x}Ag_xS$.

for the generation of $^{\bullet}OH$, which is the primary oxidizing agent in the degradation process.[58] The temperature dependence showed an optimal operating temperature of 45 °C (k = 0.029 min^{-1}), and rate constants decreased at both lower and higher temperatures (Fig. 6d). The process is highly correlated with the Arrhenius law as the temperature rises from 25 °C to 45 °C to increase the rate of charge movement and enhance surface reaction rates. High temperatures (above 45 °C) may induce surface reconstruction or alteration, thereby promoting electron–hole recombination rates and ultimately reducing photocatalytic efficiency. These optimization studies determined the optimum operation parameters (10 ppm MB, 10 mg catalyst, pH 9, 45 °C) to achieve optimum photocatalytic efficiency of $Cu_{1-x}Ag_xS$, which is useful in practical application in experimental wastewater treatment systems.

3.7 Analysis of active species and reaction mechanism

Radical-trapping experiments and electron paramagnetic resonance (EPR) spectroscopy were performed to specifically identify the role of reactive species in the photocatalytic pathway. The photocatalytic degradation of the substrate with no radical-trapping agent (as represented in Fig. 7a) had a rate constant of 0.029 min^{-1}, while the inclusion of a radical-trapping agent (P-BQ or IPA) decreased the rate constants to 0.009 and 0.013 min^{-1}, respectively, indicating that superoxide ($^{\bullet}O_2^-$) and hydroxyl ($^{\bullet}OH$) free-radical species result from the photocatalytic process.

The additional observation of significant inhibition of photocatalytic activity due to the presence of $AgNO_3$ and EDTA further suggests that both the electrons and holes generated by the photocatalytic process are necessary precursors for the formation of the radical species. The free-radical generation was confirmed by EPR spectra of both DMPO-$^{\bullet}O_2^-$ and DMPO-$^{\bullet}OH$ only under visible light, with no appearance of significant signals under dark conditions (Fig. 7b), providing direct evidence that the combined use of both radical species is responsible for the degradation of the photocatalytic substrate.[59] The photocatalytic and antibacterial properties of the $Cu_{1-x}Ag_xS$ nanocatalyst depend on the modification of its electronic structure and the control of its charge carrier density. To understand this, we first calculated the conduction band (CB) and valence band (VB) edge potentials using the absolute electronegativity of the semiconductor.

The band edge potentials of $Cu_{1-x}Ag_xS$ were calculated using the following two relations:[60]

$$E_{CB} = \chi - E_e - 0.5 \times E_g,$$

$$E_{VB} = E_g + E_{CB},$$

where χ is absolute electronegativity (6.0 for $Cu_{1-x}Ag_xS$), E_e is the free electron energy on the hydrogen scale (4.5 eV), and E_g is the band gap. The conduction band potential of $Cu_{1-x}Ag_xS$ was estimated to be about +0.71 V (*vs.* NHE), which does not allow the single electron reduction of molecular oxygen to superoxide ($O_2/^{\bullet}O_2^-$, −0.33 eV), but the formation of $^{\bullet}O_2^-$ radical was supported by EPR and scavenger tests. This apparent contradiction can be understood by the surface-controlled reduction mechanism with Ag dopants. The Ag positions act as binary centres at which molecular oxygen can be adsorbed. Substantial chemisorption of O_2 on the Ag surface decreases the activation energy and overpotential of the reduction reaction. This surface interaction stabilizes the transition state and alters the local reduction potential so that the otherwise prohibited reaction can proceed at a high rate. Plus, the current–voltage (I–V) curve of the doped material shows that charge carriers can be quickly transported to the catalyst surface once separated. This increased charge transport results in a higher reaction rate, as the photocatalytic rate constant of the doped sample (k =

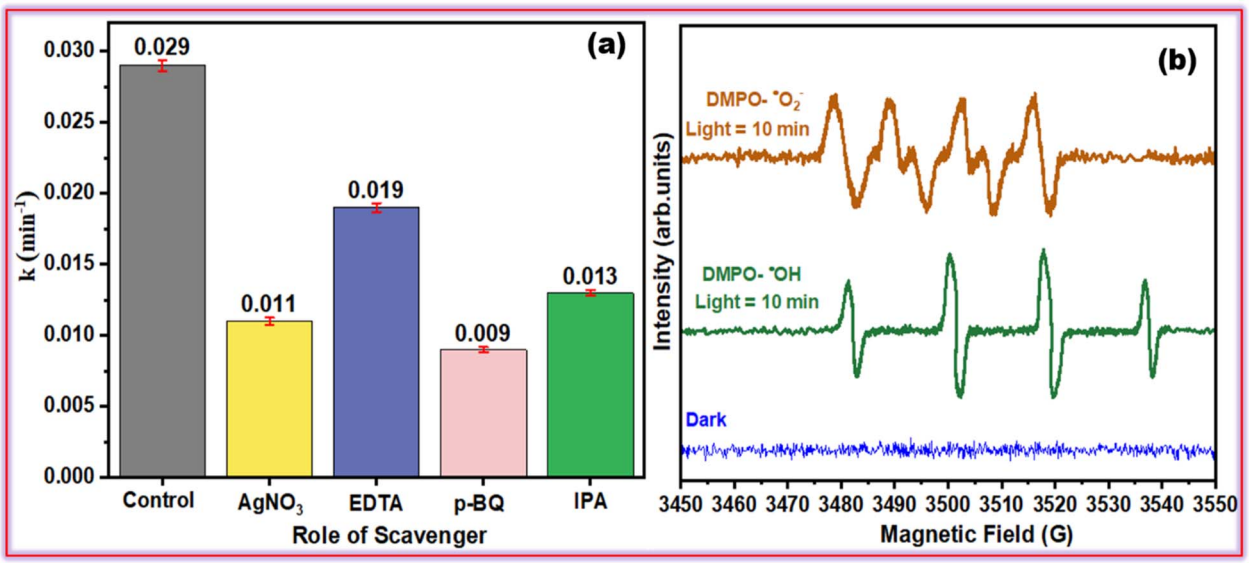

Fig. 7 Scavenger tests and EPR analysis. (a) Effects of scavengers on the rate constant k. (b) EPR signals of DMPO-$^{\bullet}O_2^-$ and DMPO-$^{\bullet}OH$ radicals in visible light.

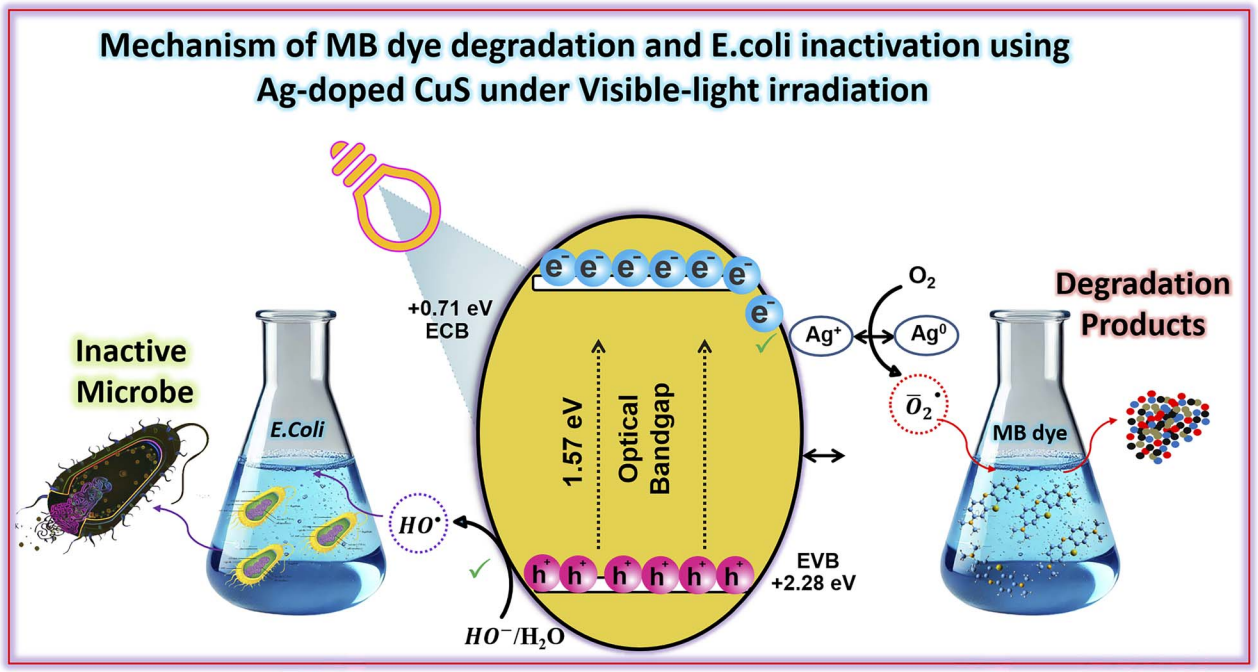

Fig. 8 Schematic of the proposed mechanism of antibacterial activity and methylene blue (MB) dye degradation facilitated by the $Cu_{1-x}Ag_xS$ nanocatalyst.

0.029 min^{-1}) is significantly higher than that of the undoped sample ($k = 0.008\ min^{-1}$).

Hence, under visible-light irradiation, the high rate of electron excitation, the optimized charge separation, and the high charge-transport rate, all facilitated by Ag doping, result in the effective formation of ROS. The Ag-mediated red shift in the band gap allows the utilization of a wide range of the visible spectrum as the initial stimulus for the photocatalytic process. The excited electrons are then effectively trapped by the Ag dopant, where they reduce adsorbed molecular oxygen (O_2) to form superoxide anion radicals ($^{\bullet}O_2^-$).[61] At the same time, the photogenerated holes (h^+) in the valence band (+2.28 eV) have a high positive potential and effectively oxidize the adsorbed hydroxyl (^-OH) or water molecules (H_2O) to form hydroxyl radicals ($^{\bullet}OH$), as $OH^-/^{\bullet}OH$ is 1.99 eV *vs.* NHE.[62,63] Fig. 8 illustrates the proposed dual-functionality mechanism for both dye degradation and bacterial inactivation. As confirmed by our scavenger experiments, the $^{\bullet}OH$ and $^{\bullet}O_2^-$ radicals play the main role in the multifunctionality of the system. These non-selective species attack the chromophore group in the MB dye and mineralize it to harmless CO_2 and H_2O. Additionally, the reactive oxygen species (ROS) create an environment of lethal oxidative stress for *E. coli* bacteria, thus degrading the integrity of the cell membrane and causing the bacteria to die. The stepwise photocatalytic reactions that occur here are as follows:

$$\text{Ag-doped-CuS} + h\nu \rightarrow e^-\ (\text{trap}) + h^+\ (\text{VB}),$$

$$e^-\ (\text{trap}) + O_2 \rightarrow {}^{\bullet}O_2^-,$$

$$H_2O/OH^- + h^+\ (\text{VB}) \rightarrow {}^{\bullet}OH,$$

$$^{\bullet}O_2^-/^{\bullet}OH + \text{MB dye} \rightarrow \text{Degraded products},$$

$$^{\bullet}O_2^-/^{\bullet}OH \rightarrow \text{Cell Inactivation}.$$

3.8 Stability and reusability assessment

To explore the reusability of the doped photocatalyst, cyclic degradation experiments were conducted over five runs. Fig. 9a clearly shows that the Ag-doped CuS maintained stable performance during the photocatalytic reactions, with only a slight decline in initial activity at the completion of five successive runs, which may be due to surface passivation or to inevitable catalyst loss during the recovery process.[64] Fig. 9b shows that the diffraction patterns of the sample before (red) and after (black) the photocatalytic experiments were almost identical, revealing that catalyst's crystal structure remains chemically and structurally stable during the photocatalytic process.

4 Limitations and future outlook

Herein, we demonstrate nanostructured Ag-doped CuS as a multifunctional material with excellent visible-light-driven photocatalytic activity for methylene blue degradation and *E. coli* inactivation which provides great potential for the simultaneous treatment of these two pollutants. However, the practical use of the as-prepared photocatalyst in realistic wastewater treatment is challenging due to the complexity of multiple pollutants and possible ion interferences. In addition, the present study is limited by the lack of ICP-AES, LSPR, and XPS analyses to obtain quantitative elemental composition, plasmonic properties, and confirmation of surface chemical states.

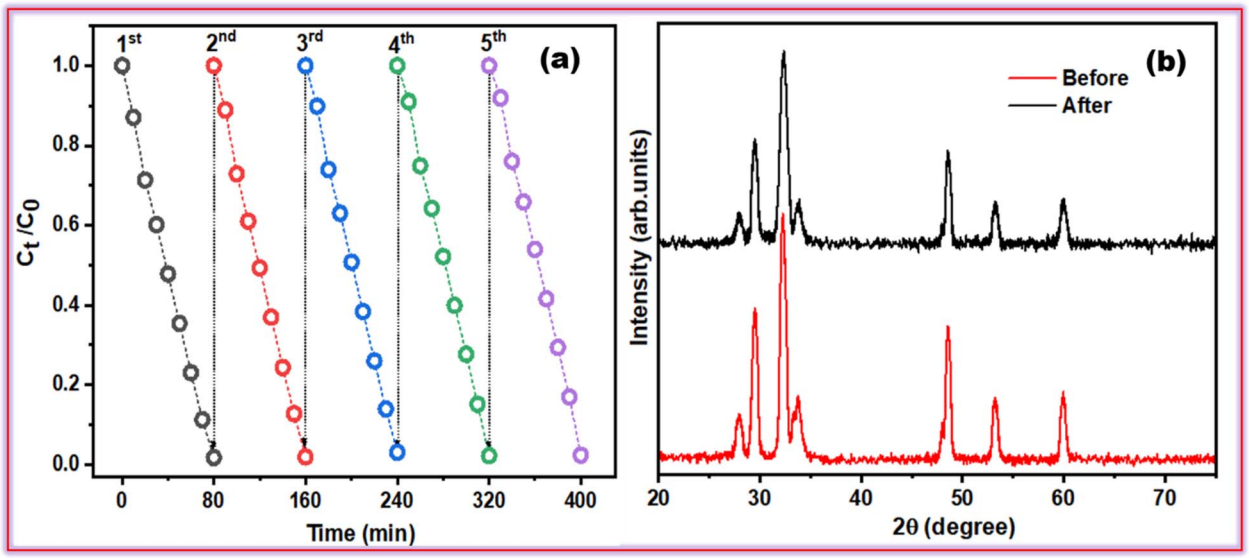

Fig. 9 (a) Reusability assessment of the Ag-doped CuS photocatalyst over five cycles. (b) XRD patterns of the fresh and used catalyst.

In the future, these gaps will be filled to the full extent to understand the degradation mechanisms and surface electronic properties.

5 Conclusions

This study was motivated by the issue of slow charge transport and fast recombination in CuS. We were interested in narrowing the band gap, modifying the structure, and enhancing conductivity through controlled Ag doping. *I–V* analyses showed that electrical conductivity was enhanced by Ag, enabling greater charge transfer and thus better results. At pH 9 and 45 °C, this silver doping in CuS significantly enhanced the degradation rate and antibacterial activity by 3.6-fold. The results indicate that lattice-selective doping converts CuS into a multifunctional photocatalyst with integrated features that simultaneously achieve efficient pollutant degradation and rapid antimicrobial aptitude.

Conflicts of interest

There are no conflicts to declare.

Data availability

Data will be made available upon request.

Acknowledgements

The authors express their gratitude to the Princess Nourah bint Abdulrahman University Researchers Supporting Project (Grant No. PNURSP2026R12) and the Princess Nourah bint Abdulrahman University, Riyadh, Saudi Arabia. The authors extend their appreciation to the Deanship of Scientific Research, Islamic University of Madinah, Saudi Arabia, for funding this research work.

References

1 A. Sahu and J. C. Poler, Removal and degradation of dyes from textile industry wastewater: Benchmarking recent advancements, toxicity assessment and cost analysis of treatment processes, *J. Environ. Chem. Eng.*, 2024, 113754.
2 J. Y. Lu, Z. Q. Bu, Y. Q. Lei, D. Wang, B. He, J. Wang and W. T. Huang, Facile microwave-assisted synthesis of Sb2O3-CuO nanocomposites for catalytic degradation of p-nitrophenol, *J. Mol. Liq.*, 2024, **409**, 125503.
3 Z. Chen, J. Li, J. Zhang, H. Wang, Y. Zeng, F. Wang, P. Huang, X. Chen, L. Ge, R. A. Dahlgren, H. Gao and X. Huang, A highly efficient and recyclable living biocatalyst using Shewanella@polydopamine@NH2-doped carbon dot biohybrids and polypyrrole immobilized melamine foam for microbial-photoreduction of Cr(VI), *J. Clean. Prod.*, 2024, **435**, 140497.
4 B. Monisha, R. Sridharan, P. S. Kumar, G. Rangasamy, V. G. Krishnaswamy and S. Subhashree, Sensing of azo toxic dyes using nanomaterials and its health effects-A review, *Chemosphere*, 2023, **313**, 137614.
5 I. Muneer, A. N. Cheema, D. Ali and F. Yasmeen, Hydrothermal synthesis of Gd-doped CaO nanoparticles from lemon peel extract for efficient photocatalytic degradation of methylene blue under UV and sunlight, *Ceram. Int.*, 2024, **50**, 54064–54075.
6 M. Al Kausor and D. Chakrabortty, Polyaniline (PANI) grafted hierarchical heterostructure nanocomposites for photocatalytic degradation of organic pollutants in waste water: a review, *Surf. Interfaces*, 2022, **31**, 102079.
7 Y. Zhang, H. Zhang, F. Chang, P. Xie, Q. Liu, L. Duan, H. Wu, X. Zhang, W. Peng and F. Liu, In-situ responses of

phytoplankton to graphene photocatalysis in the eutrophic lake Xingyun, southwestern China, *Chemosphere*, 2021, **278**, 130489.

8 A. Parsaei-Khomami, M. Mousavi, M. M. Habibi, K. Shirzad, J. B. Ghasemi, L. Wang, J. Yu, H. Yu and X. Li, Highly efficient visible light photoelectrochemical degradation of ciprofloxacin and azo dyes by novel TiO2/AgBiS2 photoelectrocatalyst, *Solid State Sci.*, 2022, **134**, 107044.

9 Y. Li, J. Bu, Y. Sun, Z. Huang, X. Zhu, S. Li, P. Chen, Y. Tang, G. He and S. Zhong, Efficient degradation of norfloxacin by synergistic activation of PMS with a three-dimensional electrocatalytic system based on Cu-MOF, *Sep. Purif. Technol.*, 2025, **356**, 129945.

10 I. A. Parray, S. A. Ali, J. Shah and R. Kotnala, Green energy generation via water splitting by non-photocatalytic process based on Gd doped magnesium ferrite hydroelectric cells, *J. Alloys Compd.*, 2024, **999**, 174951.

11 F. Xu, F. Zhao, X. Deng, J. Zhang, J. Zhang, C. Ai, J. Yu and H. García, Integrating S-scheme photocatalysis with tandem carbonylation: A green and scalable strategy for CO2 valorization, *Nat. Commun.*, 2025, **16**, 6882.

12 A. Khan, A. A. Shah, S. O. Allehabi, F. Ahmed, A. Alsulami and A. Azam, Enhanced degradation of Ciprofloxacin (CIP) antibiotic and methylene blue (MB) dye using ZnO/GO nanocomposites under solar irradiation, *Sci. Rep.*, 2024, **14**, 30696.

13 K. Pham, S. Pelisset, N. Kinnunen, P. Karvinen, T. K. Hakala and J. J. Saarinen, Controlled photocatalytic activity of TiO2 inverse opal structures with atomic layer deposited (ALD) metal oxide thin films, *Mater. Chem. Phys.*, 2022, **277**, 125533.

14 Z. Su, T. Du, J. Feng, J. Wang and W. Zhang, Clinically Approved Ferric Maltol: A Potent Nanozyme with Added Effect for High-Efficient Catalytic Disinfection, *ACS Appl. Mater. Interfaces*, 2024, **16**, 11251–11262.

15 F. Wei, H. Xing, Z. Xiu, J. Li, D. Xing and X. Han, Z-scheme TiO2-Au@ CN heterojunction for simultaneous water purification of disinfection and organic pollutant removal by simulated solar light, *Mater. Res. Bull.*, 2023, **168**, 112450.

16 J. Puneetha, N. Kottam and A. Rathna, Investigation of photocatalytic degradation of crystal violet and its correlation with bandgap in ZnO and ZnO/GO nanohybrid, *Inorg. Chem. Commun.*, 2021, **125**, 108460.

17 K. Qi, B. Cheng, J. Yu and W. Ho, Review on the improvement of the photocatalytic and antibacterial activities of ZnO, *J. Alloys Compd.*, 2017, **727**, 792–820.

18 Y. Yeszhan, K. Bexeitova, S. Yermekbayev, Z. Toktarbay, J. Lee, R. Berndtsson and S. Azat, Photocatalytic degradation of microplastics in aquatic environments: materials, mechanisms, practical challenges, and future perspectives, *Water*, 2025, **17**, 2139.

19 H. A. Alsalmah, M. Aadil and S. Zulfiqar, Hydrothermal–ultrasonication-assisted fabrication of Ce-doped ZnO/g-C3N4 heterojunctions for enhanced visible-light degradation of dye and drug pollutants, *Ceram. Int.*, 2025, **51**, 46808–46818.

20 Z. M. Aldhafeeri, M. Aadil, S. Mubeen, A. Khalid, M. R. El-Aassar, M. Hasan, M. Algarni and M. R. Alrahili, Synthesis of assembled Ag-Bi2O3/rGO composites using hydrothermal and ultrasonication and its application in drug and dye annihilation, *Ceram. Int.*, 2025, **51**, 27912–27924.

21 D. C. Onwudiwe, O. C. Olatunde, V. M. Nkwe, Y. B. Smida and H. Ferjani, Dual S-scheme heterojunction g-C3N4/Bi2S3/CuS composite with enhanced photocatalytic activity for methyl orange degradation, *Inorg. Chem. Commun.*, 2023, **155**, 111075.

22 K. Vinotha, B. Jayasutha, M. J. Abel and K. Vinoth, In3+-doped CuS thin films: physicochemical characteristics and photocatalytic property, *J. Mater. Sci.: Mater. Electron.*, 2022, **33**, 22862–22882.

23 J. Cao, D. Zhang and H. Zhang, Synthesis and photocatalytic activity of zinc-doped copper sulfide with porous nanotubes structures, *Mater. Res. Bull.*, 2024, **179**, 112990.

24 N. Ahmad, A. Alshehri, I. Ahmad, M. Shkir, P. Hasan and A. A. Melaibari, In doping effect on the structural, morphological, optical and enhanced antimicrobial activity of facilely synthesized novel CuS nanostructures, *Surf. Interfaces*, 2021, **27**, 101536.

25 H. A. Alburaih, M. Aadil, S. R. Ejaz, W. Hassan, A. Anwar, S. Anjum, S. Aman, M. S. Al-Buriahi, Z. A. Alrowaili and A. V. Trukhanov, Wet-chemical synthesis of urchin-like Co-doped CuO: A visible light trigger photocatalyst for water remediation and antimicrobial applications, *Ceram. Int.*, 2022, **48**, 21763–21772.

26 R. U. Syed, K. M. Younes, H. Banu, W. M. A. Khojali, N. A. E. Masood, F. M. Alsaiari, S. Saddeek, I. Shakir and M. Aadil, Hydrothermally synthesized W-doped CuS nanostructures with tunable structural and optoelectronic properties for redox-driven photocatalysis and antimicrobial activity, *J. Alloys Compd.*, 2026, **1060**, 187338.

27 M. K R, S. A U, K. S. Anantharaju, Y. S. Vidya, A. P. Chowdhury, K. Gurushantha and M. S, Syzygiumaromaticum Oil mediated green combustion synthesis of Ag-doped MgFe2O4 Nanoparticles: Photoluminescence, electrochemical, and photocatalytic investigations, *J. Mol. Struct.*, 2026, **1357**, 145177.

28 A. a. Ahmed Al-Adhreai, A. M. Abdulwahab, A. H. Al-Hammadi, A. Al-Adhreai, Z. A. M. Alaizeri, F. K. Alanazi, A. Salem and M. Alsaeedy, Synthesis, characterization, and photocatalytic study of Bi-doped CuS nanoparticles, *RSC Adv.*, 2025, **15**, 24483–24496.

29 H. Yang, C. Ai, Y. Zhou, B. He, J. Zhang and J. Yu, Probing the LSPR Effect of Cu-Doped ZnO Photocatalyst by Near-Infrared Femtosecond Transient Absorption Spectroscopy, *Artif. Photosynth.*, 2026, **2**, 53–66.

30 A. Q. Malik, S. Sena, D. Kumar, M. Wani and A. Rashid, Assessment of photocatalytic efficiency and antifungal activity of zinc doped copper sulfide composite embedded with graphene oxide nanosheets, *J. Mol. Liq.*, 2024, **395**, 123925.

31 M. Rejek, J. Grzechulska-Damszel and B. Schmidt, Synthesis, characterization, and evaluation of Degussa P25/chitosan composites for the photocatalytic removal of sertraline and

acid red 18 from water, *J. Polym. Environ.*, 2021, **29**, 3660–3667.

32 F. M. H. AlSulami, A. I. Al-Sulami, A. Rajeh, J. S. Alnawmasi, E. M. Abdelrazek, M. O. Farea, R. H. Aldahiri and H. M. Alghamdi, Structural, optical, dielectric and electrical properties of flexible nanocomposite based on NaAlg/PEO composite and AgNO3 NPs for energy storage applications and optoelectronic devices, *Opt. Mater.*, 2024, **152**, 115515.

33 S.-Y. Jia, Y.-J. Yang, Y.-Q. Xu, C.-J. Zheng, J. Zhang, W. Chen, M. Zhang, L. Wang and G.-B. Huang, Harnessing S-scheme charge migration in 2D/2D NaInS2/g-C3N4 heterostructures for improved photocatalytic degradation of pharmacologically active compounds, *J. Alloys Compd.*, 2025, **1020**, 179511.

34 Z. Xu, Z. Feng and Y. Xu, Preparation and characterization of R2CoMnO6 (R= La, Nd) via PVA sol-gel route, *J. Asian Ceram. Soc.*, 2021, **9**, 142–150.

35 K. Meng, J. Zhang, B. Cheng, X. Ren, Z. Xia, F. Xu, L. Zhang and J. Yu, Plasmonic Near-Infrared-Response S-Scheme ZnO/CuInS2 Photocatalyst for H2O2 Production Coupled with Glycerin Oxidation, *Adv. Mater.*, 2024, **36**, 2406460.

36 Q. Wang, S. Feng, L. Zhong, Y. Zhou, J. Liu, H. Liu and Q. Zhu, Polydopamine-functionalized cellulose nanofibrils with Ag deposition for robust poly(vinyl alcohol) hydrogel strain sensor, *Int. J. Biol. Macromol.*, 2026, **347**, 150776.

37 A. K. Chitoria, A. Mir and M. Shah, A review of ZrO2 nanoparticles applications and recent advancements, *Ceram. Int.*, 2023, **49**, 32343–32358.

38 T. Cheng, H. Gao, S. Wang, Z. Yi, G. Liu, Z. Pu, X. Wang and H. Yang, Surface doping of Bi4Ti3O12 with S: Enhanced photocatalytic activity, mechanism and potential photodegradation application, *Mater. Res. Bull.*, 2022, **149**, 111711.

39 K. H. Thamir, H. A. Ahmed, S. Z. Al-Ashoor, P. Kanjariya, M. Akku, R. Thakur, G. Jebaselvi, S. Choudhury, M. A. Rusho and H. M. Alkahtani, Hydrothermally Synthesized Fe-Doped Bismuth Oxide/CuO Nanocomposites for Efficient Photocatalytic Degradation of Rhodamine B, *J. Inorg. Organomet. Polym. Mater.*, 2025, 1–19.

40 B. Qasim, K. Jabbour, M. Ouladsmane, M. S. Waheed, M. Abdullah, N. Bano, S. Manzoor, M. Sillanpää and M. N. Ashiq, Effect of Ni dopant on the capacitive behavior of CuS for supercapacitor application, *J. Mater. Sci.: Mater. Electron.*, 2024, **35**, 445.

41 D. G. Silva, D. V. Freitas, J. A. Costa, M. C. Barros, G. B. Silva Filho, H. A. C. Bom, F. S. Mendonça, P. M. Paiva, M. Navarro and D. M. Navarro, In vivo toxicity and genotoxicity of L-glutathione capped AgIn5Se8@ ZnS nanocrystals, *Nano-Struct. Nano-Objects*, 2024, **38**, 101106.

42 A. Riaz, S. Azam, Q. Rafiq, M. T. Khan, A. U. Rahman, Q. M. Ahkam, R. Hussain and R. Khan, Vanadium-Engineered Co_2NiSe_4 nanomaterial: coupled thermoelectric, piezoelectric, and electronic optimization via DFT+ U for advanced energy applications, *Results Eng.*, 2025, **27**, 106959.

43 S. Landi, I. R. Segundo, E. Freitas, M. Vasilevskiy, J. Carneiro and C. J. Tavares, Use and misuse of the Kubelka-Munk function to obtain the band gap energy from diffuse reflectance measurements, *Solid State Commun.*, 2022, **341**, 114573.

44 V. V. Rajankumar and S. Chidambaram, Spillover enhanced CexBi1-xVO4/ByC3-yN4 S-scheme heterojunction for sustainable hydrogen production, *Fuel*, 2026, **412**, 138155.

45 R. A. Alshgari, M. Abdullah, S. I. Abbas Shah, A. G. Abid, S. Mohammad, M. F. Ehsan, M. N. Ashiq and S. I. Allakhverdiev, Enhanced photocatalytic property of Cu doped Ce2Zr2O7 toward photodegradation of methylene blue under visible light, *Heliyon*, 2024, **10**, e34266.

46 J. Xue, M. Fujitsuka, T. Tachikawa, J. Bao and T. Majima, Charge trapping in semiconductor photocatalysts: a time- and space-domain perspective, *J. Am. Chem. Soc.*, 2024, **146**, 8787–8799.

47 I. Bâldea, Y. Chen, M. Zhang, N. Xin, Y. Feng, J. Feng, C. Jia, X. Guo and Z. Xie, Breakdown of Ohm's Law in Molecular Junctions with Electrodes of Single-Layer Graphene, *J. Phys. Chem. Lett.*, 2024, **15**, 3267–3275.

48 H. A. Alsalmah, M. Aadil and S. Zulfiqar, Multifunctional Ce-In2O3@g-C3N4 nanocomposites: Synthesis, charge carrier engineering, and visible-light-driven photocatalysis, *Ceram. Int.*, 2025, **51**, 51327–51341.

49 Y. Wang, L. Li, P. Zhou, Y. Gan, W. Liu, Y. Wang, Y. Deng, H. Li, M. Xie and Y. Xu, Aeration-Free Photo-Fenton-Like Reaction Mediated by Heterojunction Photocatalyst toward Efficient Degradation of Organic Pollutants, *Angew. Chem., Int. Ed.*, 2025, **64**, e202419680.

50 F. Xu, Y. He, J. Zhang, G. Liang, C. Liu and J. Yu, Prolonging Charge Carrier Lifetime via Intraband Defect Levels in S-Scheme Heterojunctions for Artificial Photosynthesis, *Angew. Chem.*, 2025, **137**, e202414672.

51 L. Jing, Y. Xu, M. Xie, C. Wu, X. Du, H. Zhao, N. Zhong, H. Li, I. D. Gates and J. Hu, The enhanced visible-light-driven porous O/P-C3N4 for persulfate photoactivation: Enhanced removal of refractory pollutants and lignin valorization, *Chem. Eng. J.*, 2024, **482**, 149090.

52 O. H. Abuzeyad, A. M. El-Khawaga, H. Tantawy and M. A. Elsayed, An evaluation of the improved catalytic performance of rGO/GO-hybrid-nanomaterials in photocatalytic degradation and antibacterial activity processes for wastewater treatment: A review, *J. Mol. Struct.*, 2023, **1288**, 135787.

53 S. Shalini, T. Sasikala, D. Tharani, R. Venkatesh and S. Muthulingam, Novel green CQDs/ZnO binary photocatalyst synthesis for efficient visible light irradiation of organic dye degradation for environmental remediation, *J. Mol. Liq.*, 2024, **410**, 125525.

54 N. Ahmad, D. Bano, S. Jabeen, N. Ahmad, A. Iqbal, A. H. Anwer and C. Jeong, Insight into the adsorption thermodynamics, kinetics, and photocatalytic studies of polyaniline/SnS2 nanocomposite for dye removal, *J. Hazard. Mater. Adv.*, 2023, **10**, 100321.

55 M. T. Alotaibi, R. T. Mogharbel, A. Q. Alorabi, N. A. Alamrani, A. Shahat and N. M. El-Metwaly, Superior adsorption and

removal of toxic industrial dyes using cubic Pm3n aluminosilica form an aqueous solution, Isotherm, Kinetic, thermodynamic and mechanism of interaction, *J. Mol. Liq.*, 2023, **379**, 121672.

56 N. Priyadharsini, J. Manikandan, V. Jayachandran, M. Elango, A. Prasannan, R. A. Alshgari, S. Mohammad and S. Sangaraju, A systematic evaluation of physiochemical properties and solar-driven photocatalytic activity of nanosized Mn doped CdS on Methylene Blue dye, *J. Alloys Compd.*, 2024, **1002**, 175393.

57 S. Khan, T. Noor, N. Iqbal and L. Yaqoob, Photocatalytic dye degradation from textile wastewater: a review, *ACS Omega*, 2024, **9**, 21751–21767.

58 K. Michalec, B. Mozgawa, A. Kusior, P. Pietrzyk, Z. Sojka and M. Radecka, Tunable generation of reactive oxygen species in SnO2/SnS2 nanostructures: mechanistic insights into indigo carmine photodegradation, *J. Phys. Chem. C*, 2024, **128**, 5011–5029.

59 L. Jing, Y. Xu, M. Xie, Y. Liu, X. Du and J. Hu, Photothermal-assisted S-scheme PDIs/C, N, S-CeO2 derived from MOF-808 (Ce) heterojunction for photocatalytic removal of antibiotics, *J. Alloys Compd.*, 2024, **979**, 173568.

60 M. Elhadi, M. Aadil, B. Al Alwan, A. El Jery, M. R. El-Aassar, S. Zulfiqar, M. A. Rafea, A. R. Altayar and M. R. Alrahili, Enhanced physicochemical and visible-light photocatalytic properties of hydrothermally synthesized Co-doped nanostructured copper oxide, *Ceram. Int.*, 2025, **51**, 47611–47622.

61 E. B. Simsek and Ö. Tuna, Understanding the nature of Ce–Fe synergy in the structure CaWO4 scheelite for enhanced photocatalytic performance under visible light, *Ceram. Int.*, 2024, **50**, 20600–20611.

62 N. Farooq, A. ur Rehman, A. M. Qureshi, Z. ur Rehman, A. Ahmad, M. K. Aslam, H. M. A. Javed, S. Hussain, M. A. Habila and N. AlMasoud, Au@ GO@ g-C3N4 and Fe2O3 nanocomposite for efficient photocatalytic and electrochemical applications, *Surf. Interfaces*, 2021, **26**, 101399.

63 Z. Sun, P. Zhou, M. Xie, M. He, T. Zhang and Y. Xu, In-situ Sulfidation constructed oxygen-deficient FeS2/CoFe2O4 S-scheme heterojunction: Multi-metal redox synergy and defect-mediated carrier separation for ultra-efficient Imidacloprid degradation, *Chem. Eng. J.*, 2026, **527**, 171897.

64 K. Shafiq, M. Aadil, W. Hassan, Q. Choudhry, S. Gul, A. Rais, A. A. Fattah, K. H. Mahmoud and M. Z. Ansari, Cobalt and holmium co-doped nickel ferrite nanoparticles: synthesis, characterization and photocatalytic application studies, *Z. Phys. Chem.*, 2023, **237**, 1325–1344.